Supplementary Information

Tunable Multiferroic and Bistable/Complementary Resistive Switching Properties of Dilutely Li – Doped $BiFeO_3$ Nanoparticles: An Effect of Aliovalent Substitution

Mandar M. Shirolkar[1], Changshan Hao[2], Xiao Lei Dong[2], Ting Guo[2], Lei Zhang[2], Ming Li[2] and Haiqian Wang[*]

Hefei National Laboratory for Physical Sciences at the Microscale, University of Science and Technology of China, Hefei, Anhui 230026, People's Republic of China.

[1] **mandar@ustc.edu.cn, mmshirolkar@gmail.com**
[2]The authors have contributed equally to the work.
[*]Corresponding Author**:** **hqwang@ustc.edu.cn**

Experimental

All the precursor chemicals used are of analytical grade (purity ≈ 99.9%) and used as received without further purification.

In this paper, we report the synthesis of high quality pure i.e. undoped and Li^{1+} doped $BiFeO_3$ nanoparticles. We have exploited soft chemical sol – gel route reported earlier [1] in the combination with mild hydrothermal treatment for the preparation of samples. For the synthesis of pure $BiFeO_3$ equimolar mixture (5 mM) of $Bi(NO_3)_3.5H_2O$ and $Fe(NO_3)_3.9H_2O$ were dissolved in 5 N HNO_3 (69% concentration). The tartaric acid ($C_4H_6O_6$) in a equimolar ratio was added to the above mixture. The mixture was kept under mild constant stirring and heating conditions (≈ 95 ± 3^{o}C). After all the liquid evaporates, the obtained product was instantly transferred into the oven kept at 150 ± 3^{o}C for 3 hours. The product was allowed to cool to room temperature naturally. It results in fluffy greenish – brown color precipitate. The obtained powder was dispersed in water and then transferred into Teflon lined stainless steel autoclave and kept at 150 ± 2^{o}C for the hydrothermal process for 1 hour. These particles were washed with ethanol and water to remove the residual part. The XRD study shows that as prepared BFO particles are amorphous (data not shown). The crystallinity to these particles was achieved by two step process. Initially, excess NO_x impurities and hydrocarbons present in the sample were removed by preheating the sample from room temperature to 400 ± 2^{o}C at ramp rate of 2^{o}C/min and kept for 15 minutes. To achieve proper crystallinity the sample was further annealed at temperature ≈ 500 ± 2^{o}C for 2 h and cooled down naturally to room temperature. The obtained product was washed several times with Mill – Q water followed by ethanol. The powder was obtained by drying the final washed product in oven kept at 60^{o}C and ground into a fine powder. The final yield of synthesis was found to be ≈ 87% of the starting precursors.

The series of Li-doped $BiFeO_3$ nanoparticle samples were prepared by adopting the same procedure described above, however $LiNO_3$ was also added during the synthesis of Li – doped $BiFeO_3$. The concentration of $LiNO_3$ for doping in the $BiFeO_3$ was 0.2, 0.4 and 0.6 mol %. The details of characterization used is as follows.

Characterizations

The actual atomic percentage of Li in $BiFeO_3$ was determined using atomic absorption spectroscopy (AAS). Perkin Elmer Optima 7300DV spectrometer was used for this purpose.

The as prepared samples were characterized by XRD using Panalytical X'PERT PRO diffractometer. The XRD measurements were carried out at room temperature using Cu Kα radiation source ($\lambda = 1.5406$Å, operated at 40 kV and 40 mA). Data was collected in the range $2\theta = 20^o$ to 100^o with the step size 0.02^o and 10 seconds count time at each step. Samples were placed in zero background sample holder for the measurement purpose. The instrumental broadening was determined using an Al_2O_3 (corundum) sample as standard. Fullprof suite (Version September 2013) was used for Rietveld refinement [2]. The packages GFourier and Bond_Str available with Fullprof suite were used for unit cell electron density, bond angle, bond length and bond valence calculations. The refinement was carried out by following the procedure described previously [1, 3].

Raman spectroscopy of samples was carried out using HR 800 Raman spectrophotometer (Jobin Yvon, Horiba, France) using monochromatic radiation emitted by a He – Ne laser (632.8 nm) operating at 20 mW. The Raman spectra of samples were collected with a resolution of 0.5 cm^{-1}. The spectra were deconvoluted using a Lorentzian function to determine the various Raman modes.

Transmission Electron Microscopy (TEM) was performed using JEOL JEM – ARM200F. The TEM study was performed by putting a drop of dilute suspension of particles on a carbon coated copper grid.

X – ray photoelectron spectroscopy (XPS) spectra of the samples were recorded using Al Kα radiation (1486.6 eV) on a Thermo scientific ESCALAB 250. During the measurement, the base pressure of experimental chamber was $< 10^{-8}$ mbar.

Differential thermal analysis (DTA) of samples was obtained using NETZSCH Jupiter STA 449F3 instrument. The data was collected from 300 K to 1273 K at a heating rate of 2°C/min under an artificial air at pressure 60 sccm.

The magnetization measurements of the doped and undoped samples were carried out using a magnetic property measurement system (MPMS) from MPMS 5, Quantum Design Inc. San Diego, CA equipped with a 7 T superconducting magnet. The particles were packed inside a plastic sample holder, which fits into a sample holder provided by Quantum Design. We have confirmed that the magnetic signal from the sample holder was negligible and should not affect our data accuracy. We have collected room temperature M – H loops in a field sweep from -50 KOe to +50 KOe at a rate of 25 Oe/sec and data was collected at every second at the vibrating frequency of 40 Hz. The magnetic susceptibility vs. temperature (300 K – 5 K) measurements of all the samples in field cooled (FC) and zero field cooled (ZFC) conditions were performed at an applied field 200 Oe. During the measurements, the cooling and heating rate was fixed at 1.5 K/min and data was acquired at every second after averaging over 40 Hz.

Mössbauer spectroscopy of the samples was performed on the Wissel spectrometer equipped with 57Co gamma ray source (strength ≈ 50mCi embedded in Rh matrix and mean lifetime ≈ 270 days). The source has been mounted on the drive unit and the proportional counter

used as detector. The samples were nicely packed in the sample holder provided by Wissel. The study was performed in the transmission mode. The WinNorms modules associated with IGOR Pro Version 6.3 was used for fitting of Mössbauer data to extract the Mössbauer parameters.

Electric field (P−E) hysteresis loops of the samples (pellet diameter: 5 mm, with top electrode: sputtered gold and bottom electrode: silver paste). The measurements were carried out by the aixACCT TF Analyzer 2000 FE at a 1 kHz ac frequency.

Magnetic-field dependent dielectric measurements were performed using an Agilent 4284A LCR meter while the magnetic field was controlled by the above-mentioned MPMS instrument. Both the sides of the pellets were coated with silver epoxy before magnetocapacitive measurement.

The resistive switching properties of undoped and doped BFO nanoparticles were studied by depositing as prepared nanoparticles on copper metal coated glass substrate. For this purpose appropriate quantity of nanoparticles were properly dispersed in the high purity ethanol and particles were coated using spin coating. Some area of metallic copper layer was properly masked before the coating. During the deposition, the precise addition of 10 µl/s of dispersed particles was maintained for the coating purpose. The spin coating was done at the speed of 200 ± 5 rpm. By appropriately adjusting coating time in each case thickness of BFO film was adjusted to 100 ± 10 nm. The metal copper acts as the back electrode (BE) and the top electrode (TE) was made of silver metal. The mild heat treatment was given to the device (at 100^{o}C for 2 hours) to achieve better electronic contact within the device. The resistive switching behavior of the device was measured by applying a bias voltage on TE and BE grounded. The I – V data were collected using a Keithley 2420C source meter. The pulse generator Keithley 3401 was used to study the resistive switching under pulsed conditions in combination with an above

source meter. The source meter and pulsed generator were controlled by computer through LABVIEW interface. The voltage sweep during measurement was 5 mV/step.

Results and discussion

Goldschmidt tolerance factor calculations:

Goldschmidt tolerance factor is defined as [4]

$$t = \frac{\left(r_A + r_\circ\right)}{\sqrt{2}\left(r_B + r_\circ\right)} \qquad (1)$$

where r_A, r_B and $r_\circ$ represent the average ionic radii of A – cation (Bi^{3+}: 1.17, 1.40 Å in 8 and 12 fold coordination respectively), B – cation (Fe^{3+}:0.645Å in 6 fold coordination, Li^{1+}: 1.40Å in 6 fold coordination) and oxygen (O^{2-}:1.40Å in 6 fold coordination) respectively [5, 6]. Considering 12 fold coordination for A – site, for ideal undistorted perovskite $t = 1$, $0.985 < t < 1.06$ are untilted perovskite and $0.964 < t < 0.985$ shows anti – phase tilted perovskite, while $t < 0.964$ possibly shows both in – phase and anti – phase tilting.

XPS measurements:

The quality, composition and oxidation states of Bi, Fe, O and Li in the samples were obtained from XPS studies. Figure 1 shows survey scans of undoped and doped $BiFeO_3$ samples. It shows that the binding energies of Fe^{3+}: $2p_{3/2}$ and $2p_{1/2}$ spin – orbit doublets of Fe^{3+} at 711.3 and 723.8 eV (see inset of Figure 5). The absence of peak corresponding to Fe^{2+} oxidation state of iron indicates the dominant role of Fe^{3+} ions for ferromagnetism in undoped and doped $BiFeO_3$ [7, 8]. Two peaks centered at 158 and 164 eV corresponding to Bi $4f_{7/2}$ and Bi $4f_{5/2}$. It confirms the trivalent oxidation state of Bi [7]. The study also shows that the O 1s peak observed at 530.7 eV in the survey scans shows O^{2-} oxidation state of $BiFeO_3$ lattice oxygen [7, 8].

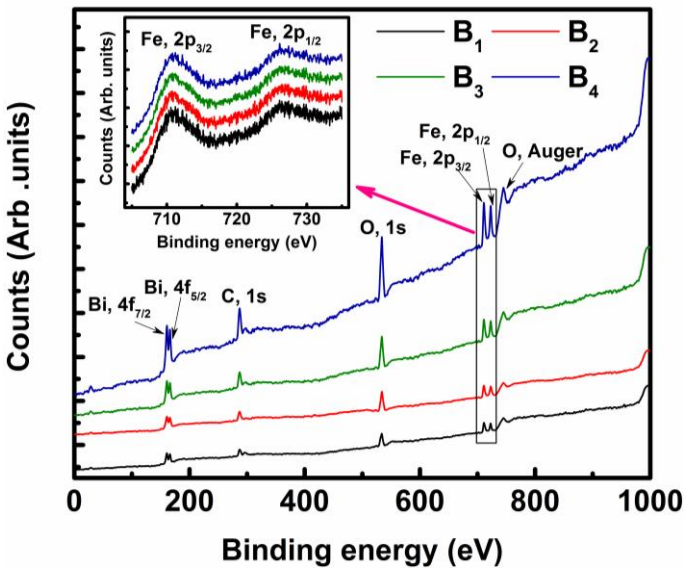

Figure 1 XPS survey scan of all the $BiFeO_3$ samples, indicating the elements present in the samples. The inset shows high resolution scan of Fe region.

The study also reveals the presence of Bi, Fe and O without any other trace of impurities except a small trace of adsorbed carbon C1s at 285 eV that was used to calibrate the system. Thus, high purity of the samples was confirmed in XPS study.

DSC measurements

It is known that doping significantly affects the ordering temperatures of $BiFeO_3$. In order to quantify it in the present case DSC study was carried out on the samples. Figure 2 shows a DSC study on the undoped and doped samples. It shows that B_1 exhibit Nèel temperature (T_N) and Curie temperature (T_C) at 645 K and 1102 K respectively, which are nearly close to the reported for BFO nanoparticles [4, 9 – 13].

On the other hand, the Li doped samples show gradual shifting of endothermic peak associated with T_N towards lower temperature, while T_C was observed to be shifted towards higher temperature. The inset in Figure 2(A) shows the variation of T_N and T_C with doping concentration. The variation in transition temperature as a function of doping concentration is attributed to chemical pressure exerted by the dopants on BFO lattice [14].

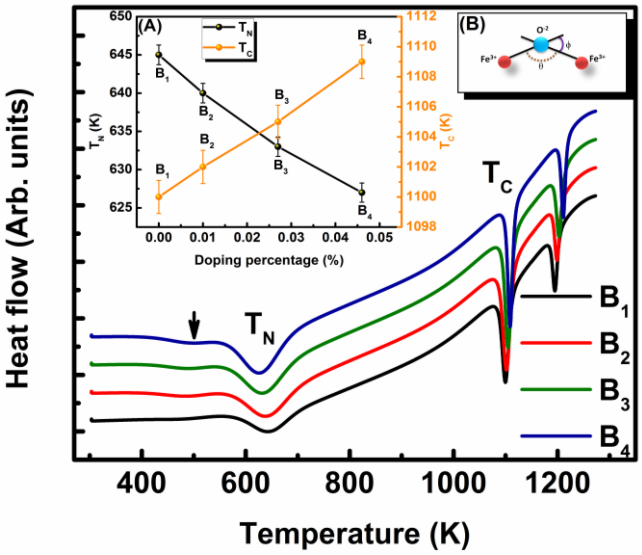

Figure 2 DSC study on undoped and doped $BiFeO_3$ nanoparticles. The inset (A) shows trend of Nèel and Curie temperature and (B) schematic representation of bending angle ϕ and bond angle Fe^{3+} – O^{2-} – Fe^{3+}. The arrow shows the magnetoelectric coupling transition.

It is known that T_N for the antiferromagntically ordered iron sublattice is proportional to (i) the number of linkages (Z) per Fe^{3+} ion, (ii) the exchange constant (J < 0) of Fe^{3+} ion pairs and (iii) the average cosine of angle θ between $Fe^{3+} – O^{2-} – Fe^{3+}$ linkages [15, 16] (as shown in the inset of Figure 2(B)). In case of BFO spin S = 5/2 for high spin Fe^{3+}, Z = 6 for FeO_6 and J is negative due to super exchange interaction. Hence, $T_N \approx JZS(S+1)\cos\theta$ [15]. It shows that T_N of BFO depends on $\cos\theta$ between $Fe^{3+} – O^{2-} – Fe^{3+}$ bond angle. As discussed earlier with the decrease in *t* value, bending angle ϕ increases, which decreases $Fe^{3+} – O^{2-} – Fe^{3+}$ bond angle, hence T_N decreases.

The variation in the rigid FeO_6 octahedra alters $Fe^{3+} – O^{2-} – Fe^{3+}$ bond angle. In Li – doped BFO, the destabilization in the anti – phase tilted ($a^-a^-a^-$) FeO_6 octahedra (as observed from Raman spectroscopy) produces a strain field around modulated FeO_6 octahedra, which results in the displacement of O^{2-}, hence T_N decreases. With the increase in the Li^{1+} doping concentration, the destabilization and modulation of FeO_6 octahedra will be more resulting in the decrease of T_N. The decrease in the T_N value for the Li – doped BFO samples can be explained on the basis of the empirical structural model proposed by Attfield et al. [17 – 20]. This model proposed that strain produced due to oxygen displacement alters phase transitions in the perovskite systems. Since, BFO is perovskite, the same model could suitably explain the observed shift in T_N values of Li doped samples.

Further, DSC study shows the gradual shifting of in the endothermic peak associated with Curie transition (T_C) towards the lower temperature side and an enhancement in the endotherm with an increase in the doping concentration. It could be explained as follows, the significant changes observed in the bond parameters, phonon modes related to Bi – O bond and oxygen ion displacement evidenced through XRD and Raman measurements collectively show that Li^{1+}

doping significantly affect ferroelectric characteristic of BFO. Hence, T_C of BFLO shifts towards lower temperature side. In addition, the results show that Li^{1+} doped samples have higher decomposition temperature compared to pure BFO.

The DSC data also show broad weak transition centered around 490 K in doped samples (shown with arrow in Figure 2). This DSC transition reported to be weak and attributed to magnetoelectric coupling [21]. The enhancement in the endotherm with the increase in the doping concentration indicates that Li^{1+} doping improves coupling between magnetic and electric components of BFO.

ZFC – FC measurements

Figure 3 shows the temperature dependence of ZFC and FC magnetization curves for undoped and doped samples, which shows that Li doping significantly affect the ZFC – FC behavior of BFO.

All the Li doped samples show bifurcation in ZFC – FC curves below room temperature, which represent blocking temperature (T_B). The T_B for doped samples was observed around 217, 255 and 295 K for the samples B_2, B_3 and B_4 respectively. We observed that below T_B, FC curve increases and ZFC curve decreases monotonically with decreasing temperature up to 70 K. It represents noninteracting superparamagnetic nature of particles. For such particles below T_B, the magnetic moments along one of the anisotropic directions are blocked and it does not respond to the applied weak field. Therefore, the magnetic properties of sample depend on magnetic history, which gives different behavior in FC and ZFC magnetization.

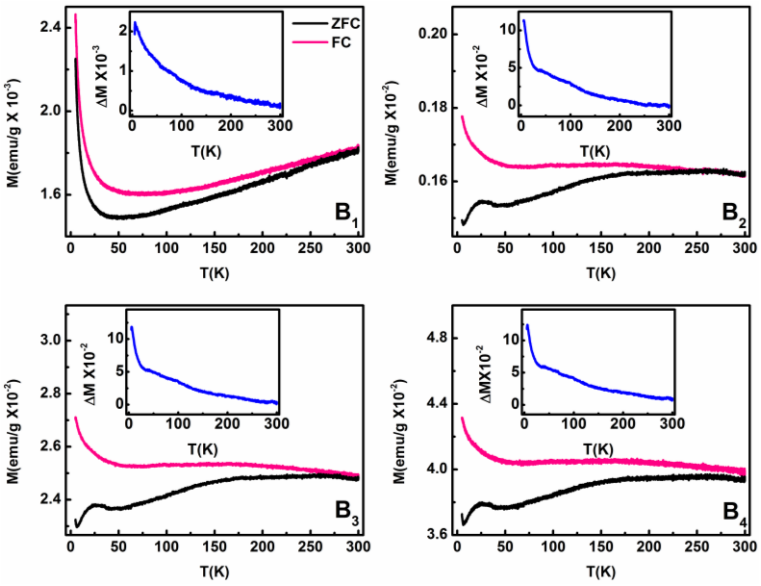

Figure 3 M - T study of undoped and doped $BiFeO_3$ samples. The inset shows difference between M_{Fc} and M_{ZFC}.

Between 70 – 40 K the ZFC curve of doped samples shows another broad decreasing trend. It represents the reorientation of Fe^{3+} moments at peak temperature. The decrease in the magnetization with decrease in temperature in FC curve is relatively higher than ZFC curve, which shows that Li – doped samples exhibit field induced phase transitions. In all the doped samples in the ZFC curve at low temperature around 25 K a sharp cusp is observed. In BFO, it represents a linear magnetodielectric coupling transition [1]. Moreover, we observed broadening in the cusp with the increase in the Li doping concentration. It infers that Li doping induces some modifications in the spin and dielectric coupling components of BFO. In all the samples, in the temperature range 7 to 5 K the rise in the ZFC and FC magnetization represents temperature induced weak ferromagnetic behavior. Some of the low temperature magnetic transitions (coupled with ferroelectric components) associated with BFO were reflected in the FC – ZFC difference plot (see inset in Figure 3(B) – (D)). It indicates that doping affects the intrinsic coupling between magnetic and ferroelectric properties of BFO. On the other hand, in the sample B_1 not much difference between FC and ZFC curves and can be observed from the inset in Figure 3(A). It shows a bifurcation around 230 K, which represent blocking temperature (T_B) and shows broad minima around 50 K. The splitting in ZFC – FC curve represent weak ferromagnetism arising from spin canting. Hence, the observed magnetic properties conclude that Li doping strategy in case of BFO enhances the magnetic properties indicating better suitability for device applications.

Mössbauer measurements

To quantify the charge state and local environment of Fe in BFO, Mössbauer spectroscopy was used. Since, it is likely that during the growth (undoped and doped BFO) due to oxygen vacancies, Fe^{3+} may perhaps reduce to other oxidation states of Fe in the lattice (most likely to Fe^{2+}) and contribute in magnetic properties of the material.

Figure 4 shows Mössbauer spectra of all the samples, which shows clear magnetic sextets splitting.

The Mössbauer parameters, namely the isomer shift (IS), quadrupole splitting (QS) and hyperfine field (B_{HF}) derived from the spectra are given in Table 1, which also shows the derived Mössbauer parameters reported by Park et al. [22] for the comparison.

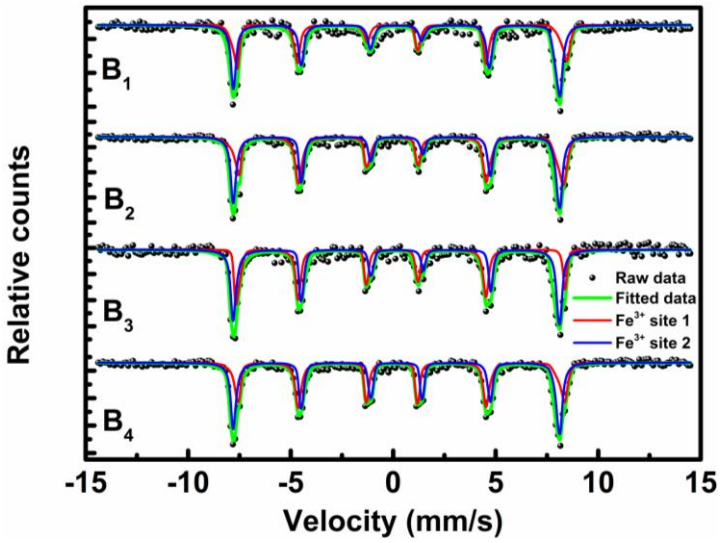

Figure 4 Room temperature Mössbauer study of undoped and doped $BiFeO_3$ samples.

The fitting reveals that iron is present in high spin Fe^{3+} state with trigonal distortion [1, 22]. This gives rise to two crystallographic environments having a small difference in the

quadrupole splitting values. The parameters obtained for undoped samples are comparable with those reported for BFO nanoparticles [22, 23].

Table 1Mössbauer parameters obtained from least square fitting of data. The table also shows reported values for the comparison.

Sample	**Fe^{3+} Site**	**Isomer Shift (IS) (mm/s) ± 0.03**	**Quadrupole Splitting (QS) (mm/s) ± 0.02**	**Hyperfine Field (B_{HF}) (KOe) ± 0.05**
B_1	1	0.40	0.72	502
	2	0.38	0.65	499
B_2	1	0.44	0.74	504
	2	0.42	0.68	502
B_3	1	0.46	0.76	509
	2	0.43	0.7	506
B_4	1	0.5	0.80	513
	2	0.47	0.73	510
51 ± 7 nm	1	0.39	0.06	484
(Ref. 61, Park et al.)	2	0.38	0.32	489

On the other hand, the obtained QS and B_{HF} values for the doped samples are relatively higher than undoped sample and show gradual enhancement with an increase in Li^{1+} doping concentration. Thus, Li doping enhances the magnetostrictive effect and affect the magnetic properties of BFO.

Magnetocapacitance measurements

The mutually exclusive ferroelectric and magnetic features of $BiFeO_3$ also give rise to the magnetocapacitance coupling properties. According to Ginzburg – Landau free energy equation, the magnetocapacitance arises due to magnetoelectric exchange interactions allowed by symmetry [24]. It is described as $\gamma P^2 M^2$, where P and M respectively represents the polarization and magnetization of the material and γ is a constant representing magnetoelectric interaction, which can be either positive or negative [24]. This coupling interaction has been observed in several magnetoelectric multiferroic materials, which gives rise to a quadratic dependence of the dielectric constant on the applied magnetic field [24 – 27].

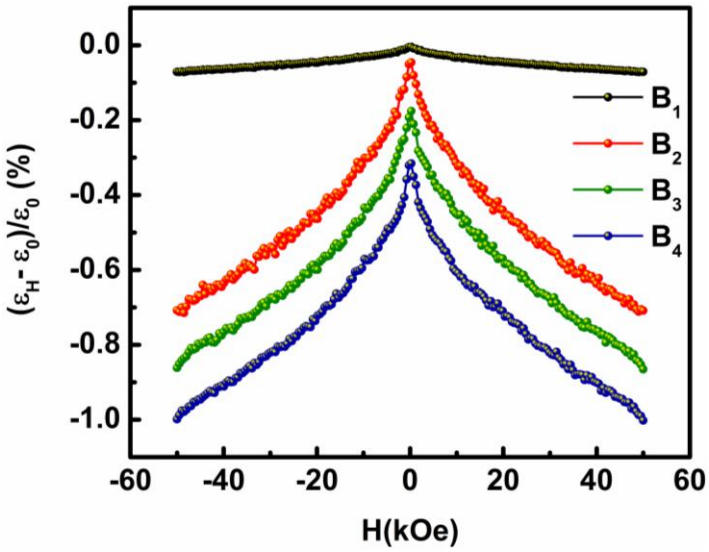

Figure 5 Room temperature magnetocapacitive measurements on undoped and Li doped $BiFeO_3$ samples.

Figure 5 shows room temperature magnetocapacitive properties of undoped and doped BFO. We observed that under applied magnetic field the undoped BFO exhibits magnetocapacitance of the order of 0.07 %, while, enhancement in the magnetocapacitance value was observed with the increase in the Li^{1+} doping concentration. The maximum

magnetocapacitance of the order of 1 % was observed in the sample B_4 at a field strength of ± 50 kOe. We observed partial linear shift in the dielectric constant with magnetization in the doped samples. The shift represents the occurrence of linear mangetodielectric coupling [24, 25, 27]. Thus, supporting the ZFC – FC measurement, which also show a peak around 25 K associated with linear magnetodielectric coupling transition. Moreover, the linear shift can also produce due to the term γ. Thus, Li^{1+} doped BFO could be a suitable candidate for the magnetodielectric based device applications.

References

1. M. M. Shirolkar, R. Das, T. Maity, P. Poddar and S. K. Kulkarni, *J. Phys. Chem. C*, 2012, **116**, 19503 – 19511 and references therein.
2. C. J. Rodriguez, Rietveld and pattern matching analysis program; Laboratoire Leon Brillouin, CEA-CNRS, France (FULLPROF (September 2013)).
3. M. M. Shirolkar, D. Phase, V. Sathe, C. J. Rodriguez, R. J. Choudhary and S. K. Kulkarni, *J. Appl. Phys.*, 2011, **109**, 123512.
4. G. Catalan and J. F. Scott, *Adv. Mater.*, 2009, **21**, 2463 – 2485.
5. R. D. Shannon, *Acta Crystallogr*., 1976, **A32**, 751 – 767.
6. P. M. Woodward, *Acta Crystallogr B*, 1997, **53**, 44 – 66.
7. D. P. Dutta, B. P. Mandal, R. Naik, G. Lawes and A. K. Tyagi, *J. Phys. Chem. C*, 2013, **117**, 2382 – 2389.
8. G. S. Lotey and N. K. Verma, *J. Nanopart. Res.*, 2012, **14**, 742.
9. S. Picozzi and C. Ederer, *J. Phys.: Condens. Matter*, 2009, **21**, 303201.
10. J. Silva, A. Reyes, H. Esparza, H. Camacho and L. Fuentes, *Integr. Ferroelectr.*, 2011, **126**, 47 – 59.
11. Y. Mao, T. –J. Park and S. S. Wong, *Chem. Comm.*, 2005, **46,** 5721 – 5735.
12. C. N. R. Rao, A. Sundaresan and R. Saha, *J. Phys. Chem. Lett.*, 2012, **3**, 2237 – 2246.
13. C. – H. Yang, D. Kan, I. Takeuchi, V. Nagarajan and J. Seidel, *Phys. Chem. Chem. Phys.*, 2012, **14**, 15953 – 15962.
14. G. Catalan, K. Sardar, N. S. Church, J. F. Scott, R. J. Harrison and S. A. T. Redfern, *Phys. Rev. B*, 2009, **79**, 212415.
15. A. Bombik, B. Lesniewska, J. Mayer and A. W. Pacyna, *J. Magn. Magn. Mater.*, 2003, **257**, 206 – 219.

16. M. A. Gilleo, *Phys. Rev.*, 1958, **109**, 777 – 781.

17. L. M. R. – Martinez and J. P. Attfield, *Phys. Rev. B*, 1996, **54**, R15622 – R15625.

18. J. P. Attfield, *Chem. Mater.*, 1998, **10**, 3239 – 3248.

19. D. C. Sinclair and J. P. Attfield, *Chem. Commun.*, 1999, 1497 – 1498.

20. J. P. Attfield, *Int. J. Inorg. Mater.*, 2002, **3**, 1147 – 1152.

21. G. L. Yuan and S. W. Or, *J. Appl. Phys.*, 2006, **100**, 024109.

22. T. J. Park, G. C. Papaefthymiou, A. J. Viescas, A. R. Moodenbaugh and S. S. Wong, *Nano Lett.*, 2007, **7**, 766 – 772.

23. K. L. D. Silva, D. Menzel, A. Feldhoff, C. Kübel, M. Bruns, A. Paesano Jr, A. Düvel, M. Wilkening, M. Ghafari, H. Hahn, F. J. Litterst, P. Heitjans, K. D. Becker and V. Šepelák, *J. Phys. Chem. C*, 2011, **115**, 7209 – 7217.

24. G. Lawes, T. Kimura, C. M. Varma, M. A. Subramanian, N. Rogado, R. J. Cava and A. P. Ramirez, *Prog. Solid State Chem.*, 2009, **37**, 40 – 54.

25. T. Kimura, S. Kawamoto, I. Yamada, M. Azuma, M. Takano and Y. Tokura, *Phys. Rev. B*, 2003, **67**, 180401(R).

26. N. Adhlakha and K. L. Yadav, *Smart Mater. Struct*., 2012, **21**, 115021.

27. A. B. Harris, *Phys. Rev. B*, 2007, **76**, 054447.